

Supplementary Materials

A high-current and tunable moisture-enabled electric generator for wireless wearable electronics

Yumei Li, Song Tian, Xiao Chen, Yifan Liao, Fan Jiang, Jin Ye, Yang He, Yingang Gui, Zheng Lian, Gang Liu, Jun Dai, Linhua Li, Jiang Chen, Sheng Liu, Renbo Zhu, Yuerui Lu, Mingyuan Gao*

Y. M. Li, S. Tian, Y. F. Liao, F. Jiang, J. Ye, Y. He, Y. G. Gui, G. Liu, M. Y. Gao
College of Engineering and Technology, School of Materials and Energy, Southwest University,
Chongqing 400715, China

X. Chen
The Institute of Oral Science, Department of Stomatology, Longgang Otorhinolaryngology Hospital of
Shenzhen, Shenzhen 518172, China
The Institute of Biomedical and Health Engineering, Shenzhen Institutes of Advanced Technology
Chinese Academy of Sciences, Shenzhen 518055, China.

J. Chen
The Department of Ophthalmology, Sichuan Provincial People's Hospital, University of Electronic
Science and Technology of China, Chengdu 610000, China

Z. Lian, J. Dai
School of Mechatronical Engineering, Beijing Institute of Technology, Beijing 100081, China

L. H. Li
Kidney Research Laboratory, Department of Nephrology, West China Hospital of Sichuan University,
Chengdu 610041, China

S. Liu
Institute of Technological Sciences, Wuhan University, Wuhan, 430072, China

R. B. Zhu
Research Institute for Intelligent Wearable Systems, the Hong Kong Polytechnic University, Hong
Kong, 999077, China

M. Y. Gao and Y. R. Lu
School of Engineering, College of Engineering, Computing and Cybernetics, the Australian National
University, Canberra, ACT, 2601, Australia

*Corresponding author: goalmychn@gmail.com

Supplementary Note 1: Strategic selection of material portfolios for the MEG

We employ a hydrophilic, stable material with abundant carboxyl groups and robust adhesion properties for a water-volatile functional layer. Furthermore, large ultra-thin films can be shaped from the Graphene oxide (GO)/ Polyvinyl alcohol (PVA) /Polyethylene glycol (PEG) flakes, lending itself to flexible device integration and patterning. The highly conductive Ag bottom electrode, with its low resistance, allows for unhindered diffusion of protons disassociated from the functional groups, leading to a substantial boost in short-circuit current. The silver paste coating further improves adhesion to the substrate and augments the functional layer's bonding, a key advantage over conventional Indium Tin Oxide (ITO) and Fluorine-doped Tin Oxide (FTO) electrodes. Notably, the Ag electrode's fabrication process is streamlined, efficient, and amenable to large-scale production.

When benchmarked against mainstream ITO and FTO electrode materials, Ag electrodes offer superior features: 1) Ag paste coating adheres closely to the substrate, enhancing stability and mitigating the detachment issues faced by ITO and FTO deposited via magnetron sputtering. 2) It offers superior conductivity, ductility, and stability at a low cost, outpacing ITO and FTO's cost and stability challenges for high-performance, large-scale, flexible applications. Moreover, ITO's strong water absorption can lead to spoilage due to chemical reactions with moisture and carbon dioxide. 3) Ag electrodes can be easily and efficiently mass-produced via dispensing and pressure-coating methods, sidestepping the need for complex, difficult-to-operate equipment.

GO shares the same two-dimensional planar structure and atomic layer configuration as graphene. With its oxygen-rich functional groups and excellent hydrophilicity, it plays a pivotal role in the energy conversion process of the functional layer. PVA, characterized by numerous carboxyl groups and

superior adhesion properties, could enhance the adhesion and flexibility of the functional layer. As a high molecular polymer, PEG has excellent lubricity, moisturizing, dispersion, and adhesion. Adding an appropriate amount enhances the overall plasticity, lubricity, and hygroscopicity of the functional layer.

Supplementary Note 2: Logic of the PMIC and the BLE

The Power Management Integrated Circuit (PMIC) continuously monitors the voltage of the energy storage capacitor as a reference for charging or discharging. When the external energy source initiates input to the power management (PM) circuit, energy is first stored in the energy storage capacitor, causing the capacitor voltage to rise until it reaches the set output upper voltage (**Supplementary Figure 13**). The PMIC then connects the energy storage capacitor directly to the external output port using an internal switch to enable external output. Subsequently, the capacitor voltage decreases to the lower output limit, at which point the PMIC halts external output. During external energy input, the capacitor voltage fluctuates as it alternates between charging and discharging states. Once the external energy ceases, the capacitor discharges, and the circuit powers down to ground potential, concluding its operation. This straightforward architecture ensures high energy efficiency.)

The BLE device is periodically awakened by the real-time clock (RTC). Upon waking, the BLE System on a Chip (SoC) initializes the corresponding peripherals and the Bluetooth core. It then proceeds to capture the analog voltages of the specified pins via the Analog-to-Digital Converter (ADC). Once the analog voltage is obtained, the BLE SoC invokes the relevant procedure to bundle the data into the Bluetooth broadcast data. This data is then broadcasted to the external world using an unconnectable broadcast that conveys the analog voltage value. Following this, the BLE SoC returns to sleep mode after completing the necessary RTC configurations, awaiting its next activation. The BLE device utilizes a

chip-scale DA14531 minimal system, comprising a 1M Flash and a high-performance on-board antenna within an area of $5\text{mm} \times 4.75\text{mm}$. This compact arrangement enhances system integration.

Operation process: The strain gauge is connected in series with a fixed resistance chip resistor. The voltage signal from the strain gauge is amplified by an in-phase operational amplifier and directed to the ADC sampling pin of the BLE SoC, serving as an indicator of the bending condition. Various Bluetooth devices, including those BLE devices employed in the monitoring system, can broadcast the data packet. The application utilizes a smartphone's Bluetooth module to continuously scan these packets. Since all BLE devices used in the monitoring system share the same Universal Unique Identifier (UUID), it can be utilized to recognize packets sent from BLE devices. Subsequently, based on specific rules, sensor data is extracted from the identified packets and displayed on-screen. This allows users to view the extracted sensor data in real-time and save it for further analysis when necessary.

This project is built upon the APP Inventor framework, offering a simple and user-friendly method to develop Android phone applications. By leveraging the Bluetooth module and UUID recognition function, the application can effectively gather and process BLE broadcast data, providing users with a convenient means to monitor and record sensor data.

Supplementary Note 3: First-principles calculations

To investigate the influence of PEG and PVA on GO, we chose GO fragments containing -OH and bridged oxygen, respectively, for modeling. Since both PEG and PVA are chain structures, our modeling focuses on understanding their interaction sites with GO. Hence, we selected suitable fragments for our study, as depicted in **Supplementary Figure 23**.

In **Supplementary Figure 23**, it's evident that PEG and GO-O, as well as PVA and GO-OH, form

covalent bonds through functional groups, increasing their binding energy. The stress and strain at the binding interface lead to the recombination of the surface local electronic structure of GO, enhancing the interaction and contributing to the relatively high total binding energy.

By comparing the binding energies in Table S2, we observed that PEG tends to interact more readily with the bridging oxygen position of GO, forming a relatively stable structure. Conversely, PVA shows a preference for interacting with the hydroxyl group of GO. Thus, we focused our discussion on GO-O/PEG and GO-OH/PVA fragments. **Supplementary Figure 23B** illustrates that PEG and GO-O, as well as PVA and GO-OH, form covalent bonds through functional groups, thereby increasing the binding energy of the two. The stress and strain at the binding interface lead to the recombination of the local electronic structure of GO's surface, thereby enhancing the interaction. Consequently, the total binding energy may be relatively high.

Examining the electrostatic potential in **Supplementary Figure 23C**, we note that intermolecular charge transfer or polarization effects may influence the surface structure of GO, especially when interacting with organic molecules bearing strong electron donor or acceptor groups. The COO-group formed by the oxygen atom and surrounding atoms exhibits high electronegativity, attracting and retaining more electrons, resulting in a negative potential. At the sites where PEG and GO-O bond, as well as PVA and GO-OH bond, there may be a transfer of electron density from adjacent hydrogen or carbon atoms to oxygen atoms, intensifying the negative potential around oxygen. Hydrogen atoms, with lower electronegativity, lose electron density when combined with more electronegative atoms like oxygen, potentially forming hydrogen bonds with nearby oxygen atoms. This interaction enhances the formation of a positive electric potential. The negative potential around the COO- group and the positive potential

around the hydrogen atom suggest these regions are active parts of intermolecular interaction. Oxygen atoms serve as potential electrophilic attack sites, while hydrogen atoms may participate in hydrogen bond formation, influencing structural arrangement and stability. A robust hydrogen bond network can increase the mechanical stability of materials.

To delve deeper into its conductive properties, we analyzed the Band structure and Density of States (DOS) of the fragment, a crucial step in understanding its electronic structure and conductivity. However, it's important to note that the calculations with the generalized gradient approximation (GGA), particularly the Perdew-Burke-Ernzerhof (PBE) functional, have certain limitations in predicting band gaps accurately. Generally, the PBE functional tends to underestimate the band gap of semiconductors and insulators due to its inability to adequately account for electron-dependent effects, especially long-range electron interactions. In our study of graphene oxide (GO-O) fragments, the band gap values calculated using the PBE functional were higher than anticipated, possibly due to an overestimation caused by the inadequate description of electron localization in oxygenated materials. Therefore, our band gap results should be considered qualitative, as presented in Table S2.

We observed a decrease in the band gap from 5.165 eV to 3.506 eV upon introducing PEG into the GO-O fragment. This reduction indicates an increase in electronic state density, particularly near the Fermi level. The presence of stable chemical bonds between oxygen atoms in the PEG molecule and bridge O on the GO surface likely promotes trans-band electron jumps, contributing to this decrease.

Similarly, introducing PVA into hydroxyl-containing GO-OH fragments led to a reduction in the band gap from 5.017 eV to 4.045 eV. While not as significant as with PEG, this reduction suggests that the interaction between PVA and GO-OH facilitates easier electron migration between valence and

conduction bands. The effect of PVA may primarily manifest in altering the local electronic environment through hydrogen bonding between its hydroxyl group and GO-OH.

Supplementary Figure 23B illustrates the total state density, representing the number of electron states available at each energy level within the material. This parameter reflects electron localization, band gap size, and possible electron transitions. Notably, the addition of PEG facilitates electron transitions from the valence band to the conduction band. In the valence band region, the contribution of *p*-orbital electron states of oxygen and carbon atoms dominates the partial wave state density. This underscores the importance of these atoms' *p* orbitals in chemical bond formation, crucial for determining material properties such as optical properties and reactivity. Conversely, in the conduction band region, the dominance of the oxygen atom's *p*-orbital electron states suggests high reactivity or strong electron-electron interaction, possibly influenced by oxygen's high electronegativity and electron repulsion.

Comparing PEG/GO-O to GO-O, we observe a wider distribution of PDOS in PEG/GO-O, indicating dispersed electron states. This expansion may result from structural relaxation or the introduction of impurity states due to PEG, affecting electron localization, conductivity, and photoelectric properties. These findings are crucial for understanding the electronic structure and potential properties of PEG/GO-O composites, including electronic, photoelectric, and chemical properties. The dominant role of the oxygen atom's *p*-orbital in the conduction band suggests potential activity in REDOX reactions. Additionally, the introduction of PEG enhances the dispersion of electronic states compared to GO-O, potentially improving electron transport performance.

For PVA/GO-OH fragments (**Supplementary Figure 23C**), the significant contribution of *p*-orbital electrons emphasizes the role of π and σ bonds in regulating material optical properties and

electrochemical activity. Above 0 eV, the dominance of the oxygen atom's *p*-orbital electron state, likely due to its high electronegativity, suggests its crucial role as a bridge between electrons, especially in REDOX reactions. The enhancement of the oxygen atom's *p*-orbital electron states, particularly in the conduction band, implies improved electron activation and migration abilities, potentially enhancing material conductivity and catalytic activity.

In the PVA/GO-OH composite, the wider distribution of the carbon atom's PDOS indicates dispersed electrons in energy, possibly due to structural changes induced by PVA introduction. Simultaneously, the denser electron distribution of oxygen atoms in the conduction band region suggests that PVA addition significantly enhances the role of oxygen atoms in facilitating electron transport and catalyzing reactions. These results underscore the significant impact of PVA addition on the electron state distribution of oxygen and carbon atoms in GO-OH, potentially improving material activity in REDOX reactions and enhancing electron migration performance and overall conductivity.

Supplementary Note 4: Electric generation mechanism of the MEG

Liu et al. ¹ performed a detailed analysis of the humidity power generation mechanism. Even though the functional material in their study comprised protein nanowires, the internal diffusion movement of H⁺ ions remained consistent. Building on this foundational understanding, we undertook an analysis of the operational mechanism of the MEG.

The diffusion current density of H⁺ can be expressed as:

$$J_{diff} = -qD \frac{dC}{dx}$$

#E1

Where q and D represent the carrier charge and the diffusion coefficient, $\frac{dC}{dx}$ represents the gradient of proton concentration along the thickness of the film.

The drift current density generated by the electric field can be expressed as:

$$J_{drift} = \sigma^{nw} \cdot E \quad E2$$

Where σ^{nw} and E represent the electric conductivity in the GO/PVA film and the electric field strength of the equilibrium electric field.

When diffusion reaches equilibrium, the drift current density is equal to the diffusion current density:

$$J_{drift} = J_{diff} \quad \#E3$$

$$-qD \frac{dC}{dx} = \sigma \cdot E \quad \#E4$$

At this time, it is an open circuit state, and the potential difference between the top and the bottom is the open circuit voltage V_0 , and E is the electrostatic field generated by this open circuit voltage. The thickness of the GO/PVA is thin (several μm), and therefore the charge distribution can be approximately regarded as linear:

$$\frac{dC}{dx} = \frac{\Delta C}{h} \quad \#E5$$

$$E = \frac{V_0}{h} \quad \#E6$$

Combined with equation E1, the open circuit voltage V_0 can be written as:

$$V_0 = \frac{qD}{\sigma} \Delta C \quad \#E7$$

From the derivation of the open circuit voltage, it can be found that:

(a) The open circuit voltage is independent of the thickness of the material.

(b) The open circuit voltage is positively correlated with the charge difference between the bottom surface and the top surface, that is, positively correlated with the concentration difference.

Electric current: In our device, the reverse drift movement is constantly at play, leading to variations in current. At a steady state, the device achieves an equilibrium between drift and diffusion currents. Upon the establishment of a moisture gradient, significant electron diffusion occurs alongside minimal drift current and reverse drift movement. These factors contribute to current fluctuations but do not substantially affect the overall electrical output. The diffusion current, driven by thermal energy without a specific direction, results from concentration gradients². Variations in humidity create a gradient in the concentration of dissociated electrons, predominantly involving ion diffusion. Conversely, the drift current is generated by an internal electric field and involves only a few carriers, showing minimal sensitivity to changes in humidity. The dominant forward voltage from carrier electrons suppresses the internal electric field, enhancing the diffusion current and reducing the drift current. As a result, the prevailing direction of the current in our device aligns with the direction of the diffusion current **(Supplementary Figure 24)**.

The output current is a subset of the drift current. However, the electric field only exists within a certain distance inside the material. Consequently, if the bottom electrode, constructed using traditional surface connection techniques such as magnetron sputtering, is excessively smooth, it can be challenging to facilitate the drift current's output. When measured, the multimeter's tip can detect a substantial current, an effect not present on a smooth electrode surface. Additionally, the smooth surface prevents a close fit with the functional layer material. To resolve this issue, we prepared the bottom electrode via a scraper-

pressure-coating technique. As previously discussed, the electrode's material also plays a significant role in influencing the internal resistance. We improved not only the electrode material but also the electrode's roughness. As a result, the short circuit current of a single device increases to 623 μA .

The output current is a component of the drift current's resistance shunt,

$$I_{drift} = J_{diff} = A \cdot q \cdot D \frac{\Delta C}{h} \quad \#E8$$

The resistance shunt is defined as follows:

$$I_{out} = \frac{R_{nw}}{R_{nw} + R} \cdot I_{drift} = \frac{R_{nw}}{R_{nw} + R} \cdot A \cdot q \cdot D \frac{\Delta C}{h} \quad \#E9$$

Where R_{nw} and R represent the inner resistance of the GP/PVA film and the external load resistance.

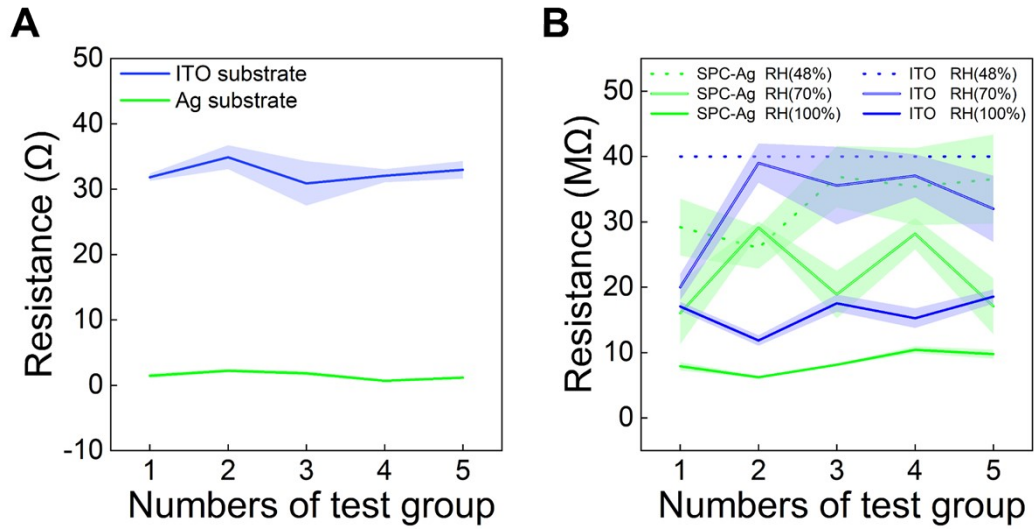
Supplementary Note 5: Simulation model of the MEG

The simulation is conducted using the COMSOL software. We utilize the Nernst-Planck-Poisson equation under the chemical substance transfer module. This equation is deployed to create a dynamic model for calculating the interplay between the electromagnetic and diffusion fields.

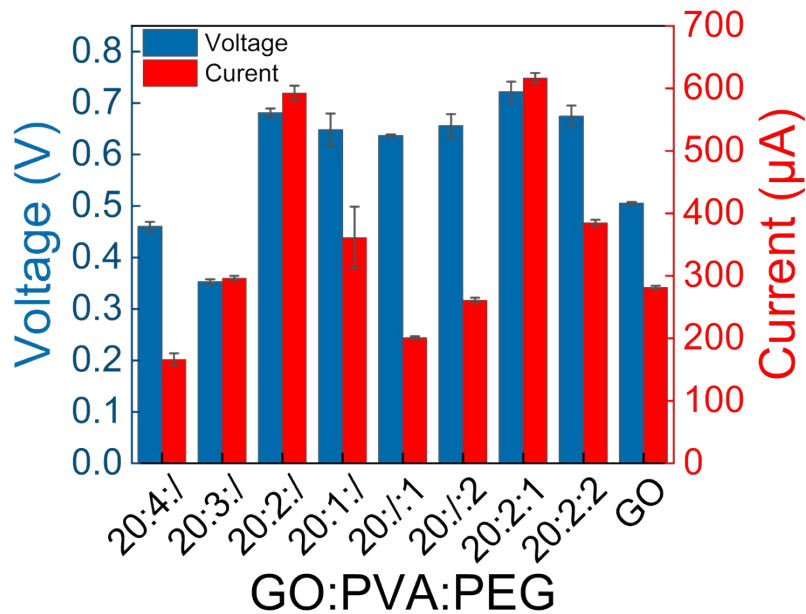
The potential of the MEG device stems from the ion concentration gradient on its vertical gradient. To simplify this, we opt for a two-dimensional structure for simulation purposes, instead of a three-dimensional structure. Within the dilute matter transfer module, we define the diffusion coefficient and establish the initial value of H^+ to correspond with the function *int1*. According to this function, the concentration of hydrogen ions increases linearly from the bottom edge to the top edge.

The space charge density throughout the entire region is defined by the equation $F_{const} * 1 * H - F_{const} * 1 * COO$. This equation presents the space charge as the charge of the

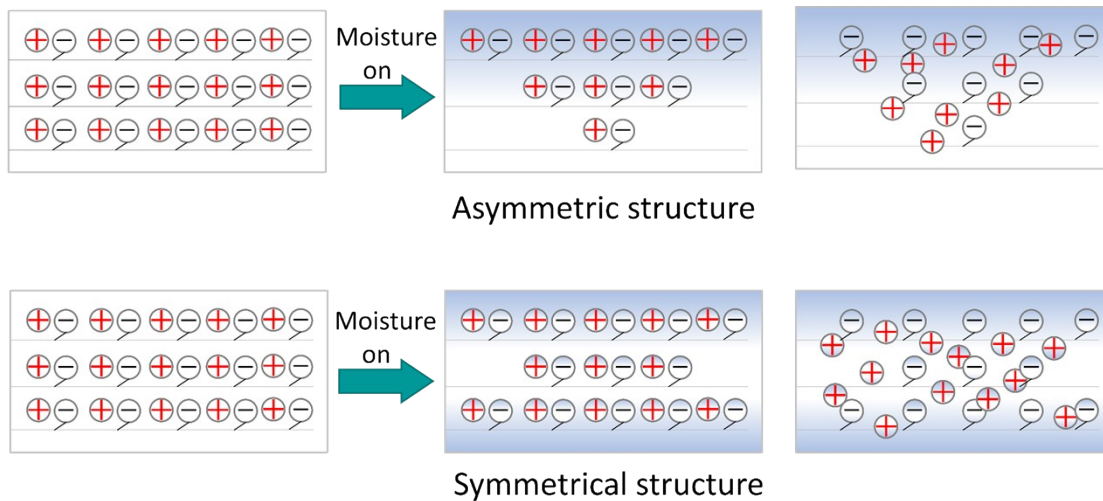
hydrogen ion minus the charge of the COO^- . Notably, the COO^- is fixed onto the graphene's carbon skeleton and is immobile. As such, it only contributes to the electromagnetic field and is excluded from the diffusion field. Therefore, we use the space charge density interface within the electromagnetic field module to represent the presence of the COO^- .



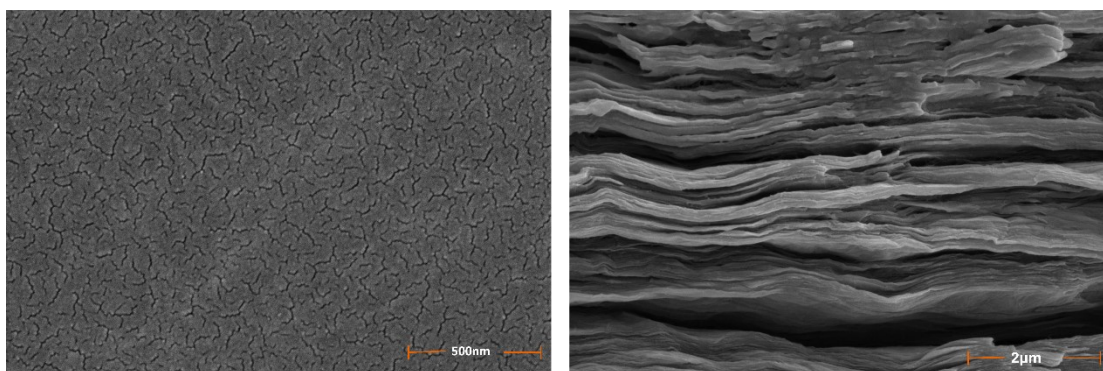
Supplementary Figure 1 Contact resistance. (A) Substrate resistance. (B) Resistance of the MEG with different substrates. SPC: Scraper-pressure-coating. The shaded area indicates the measured error range.



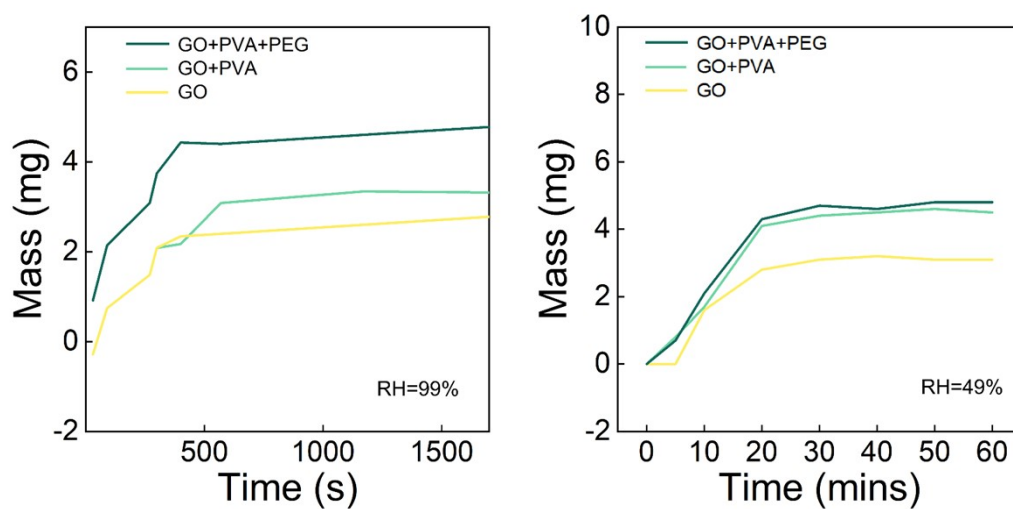
Supplementary Figure 2 Performance at different ratios of the GO/PEG/PVA system.



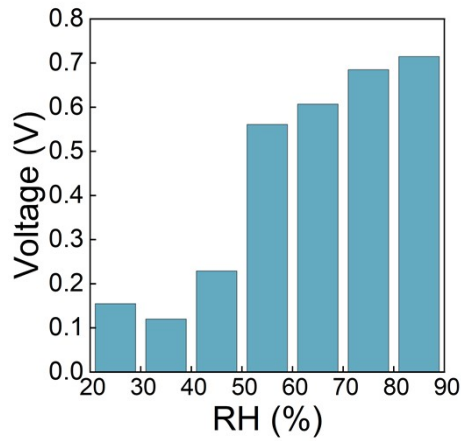
Supplementary Figure 3 Asymmetric structures form gradient dissociation of functional groups.



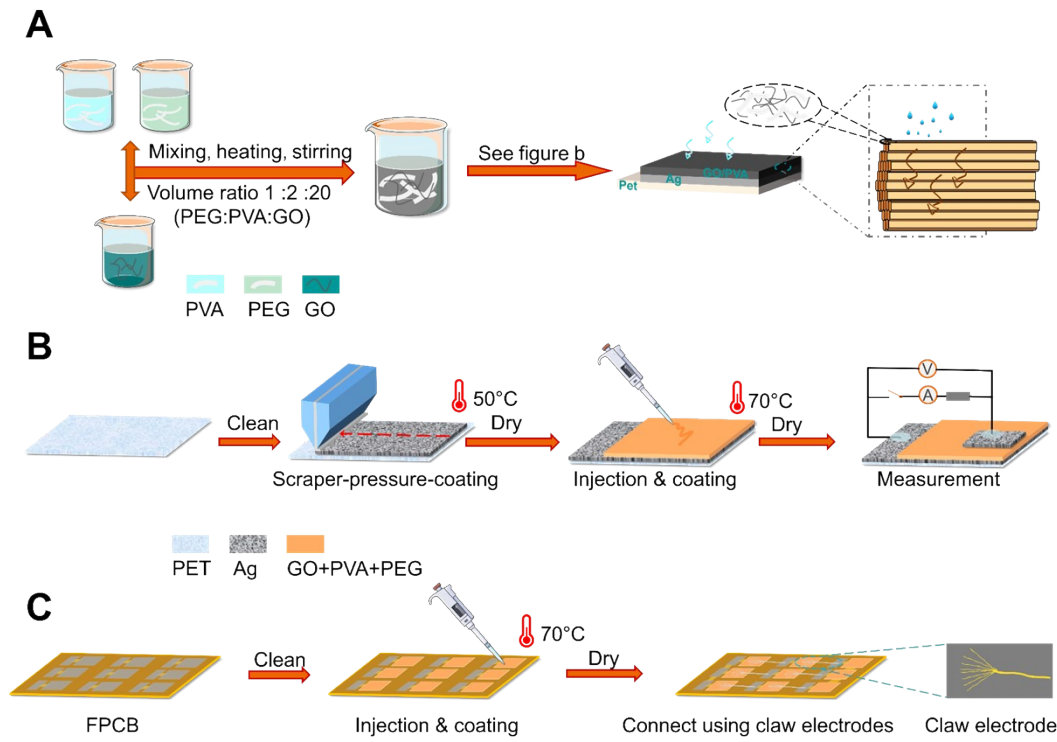
Supplementary Figure 4 SEM image of the functional layer material. The left panel indicates the surface, and the right panel is the cross-section view.



Supplementary Figure 5 Comparison of water absorption of different material components under different humidity conditions.

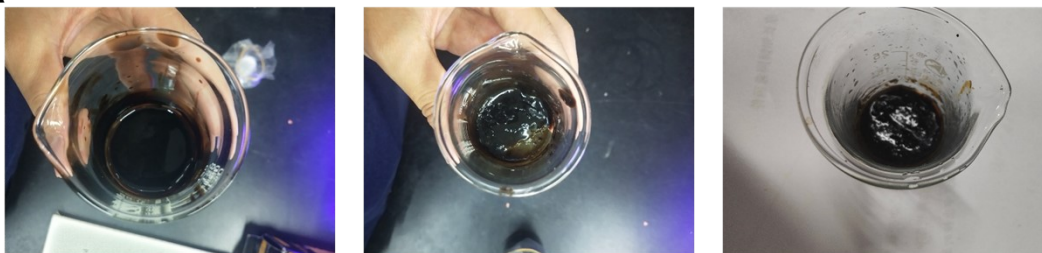


Supplementary Figure 6 Voltage output of the MEG device under different humidity conditions.



Supplementary Figure 7 Process for the fabrication of a MEG functional unit. (A) Preparation of the GO/PVA compound and the MEG. (B) Fabrication process of the MEG. (C) Fabrication process of the MEG based on the FPCB.

A

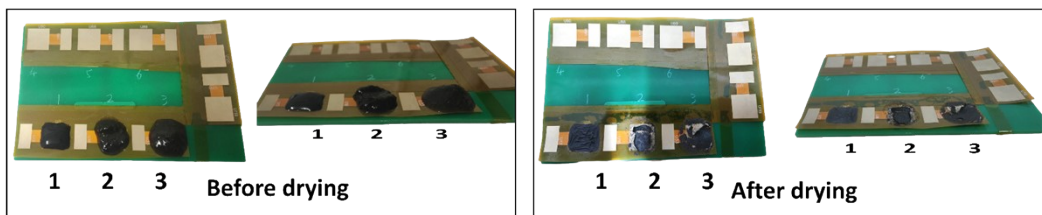


1. Ratio : GO:PVA:PEG=20:(2~4):(1~2)

2. Ratio : GO:PVA:PEG=20:>4:1

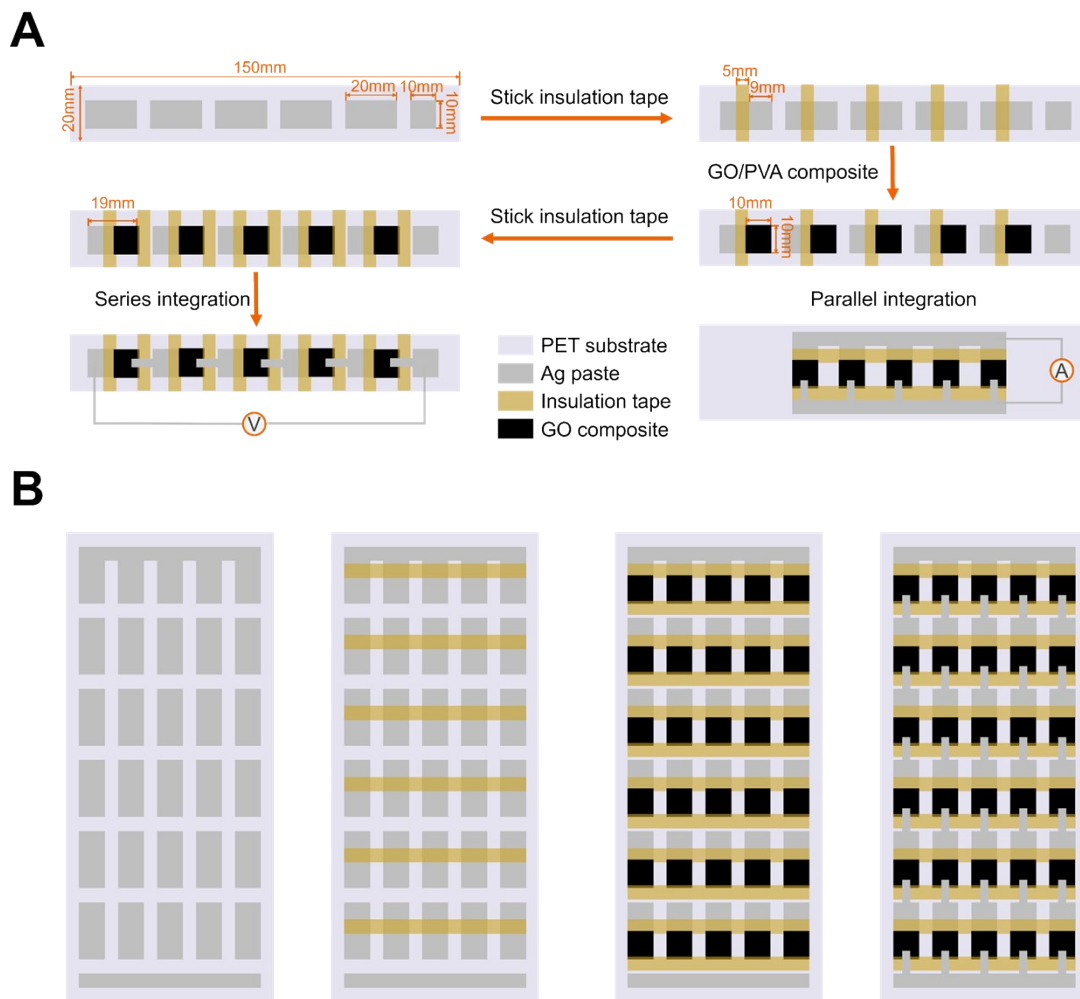
3. Ratio : GO:PVA:PEG=20:2:>2

B

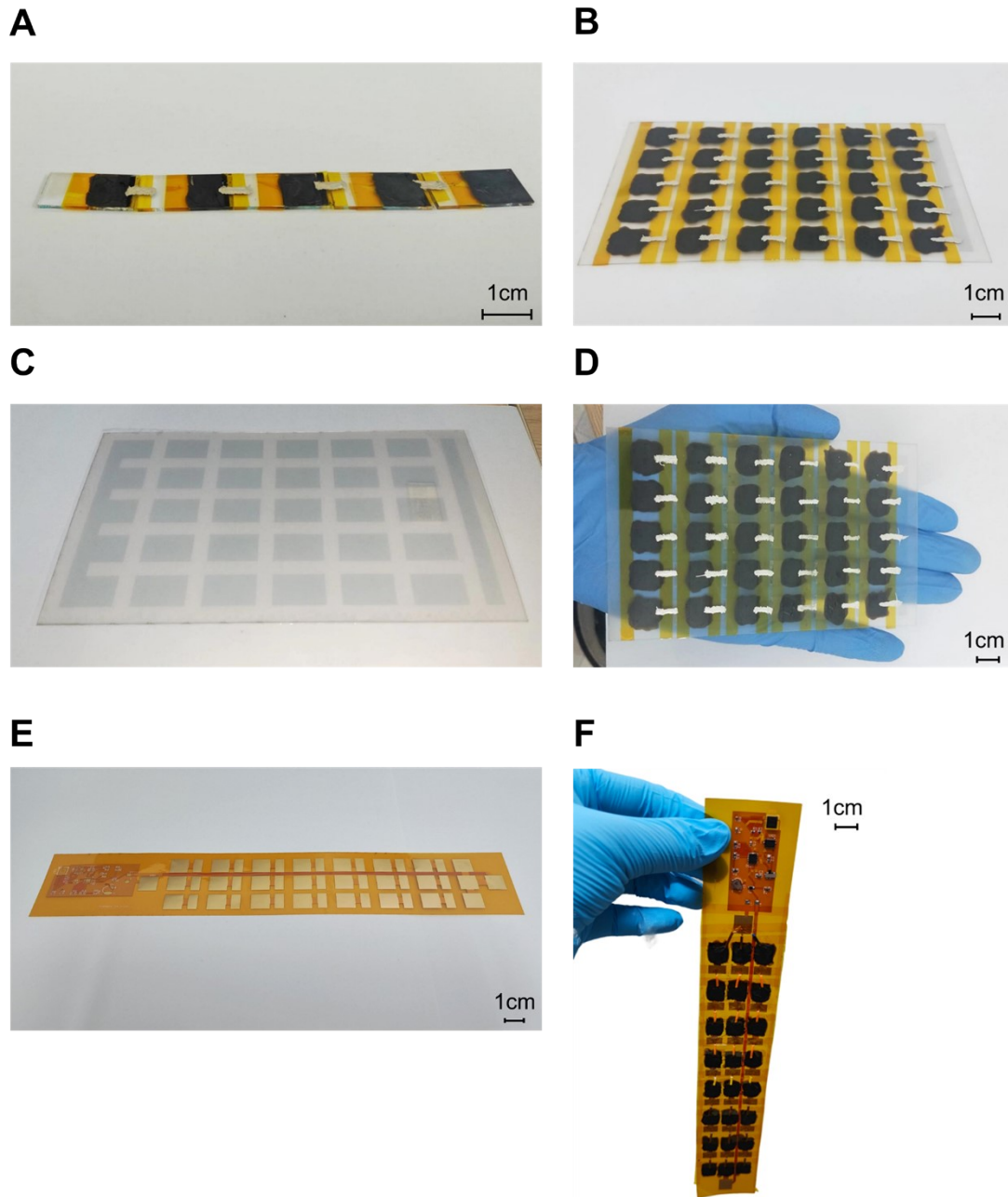


Supplementary Figure 8 Impact of varying material ratios on the condition of the functional layer.

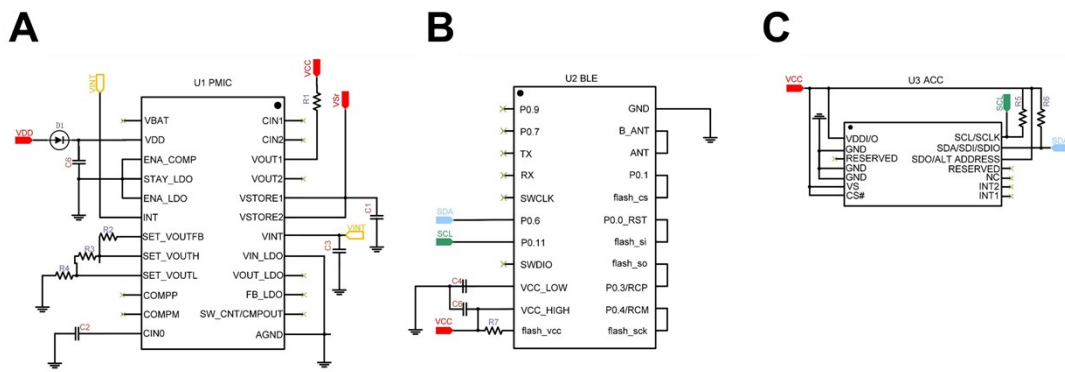
(A) Contrast diagram of different proportions of functional layer materials in liquid state. (B) Contrast diagram of different proportions of functional layer materials on the substrate.



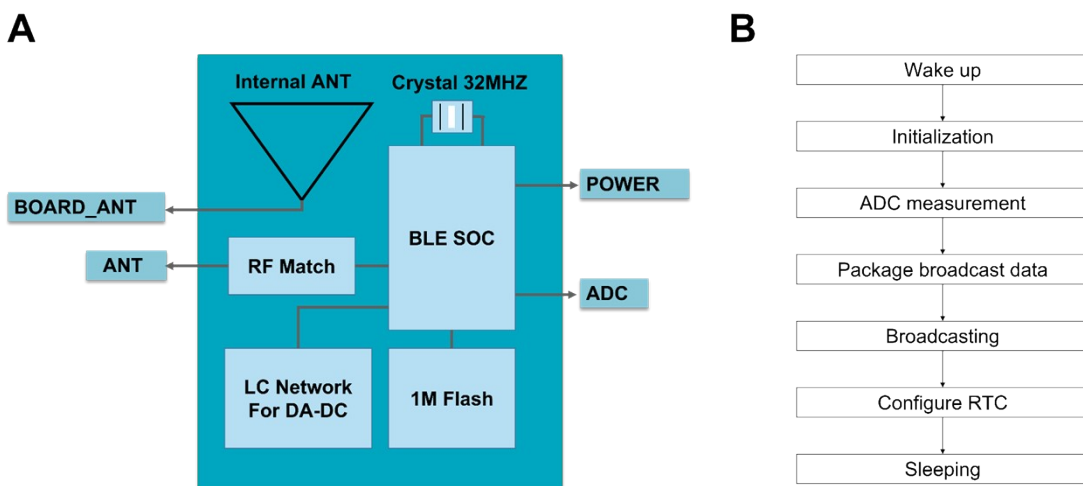
Supplementary Figure 9 Flow chart of MEG series-parallel integration. (A) Diagram of series and parallel integration. (B) Diagram of series-parallel integration (5×6).



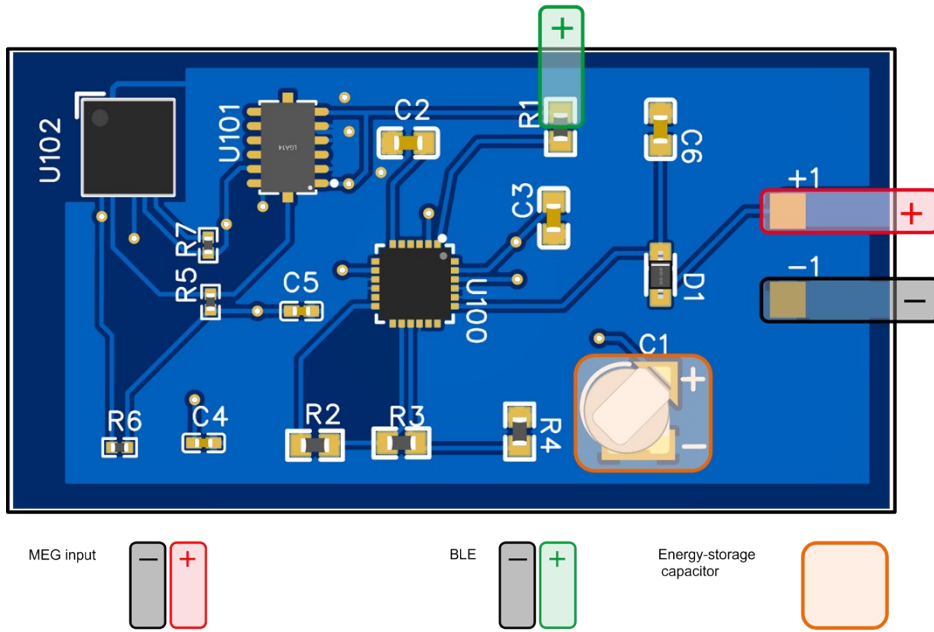
Supplementary Figure 10 Optical image of MEG series-parallel integration. (A) Optical image of series integration (5 units). (B) Optical image of series-parallel integration (5×6 units). (C) Optical image of the bottom electrode arrangement. (D) Light transmission of the device. (E) Optical image of the electrode layout on the FPCB. (F) Optical image of the MEG device with BLE transmission.



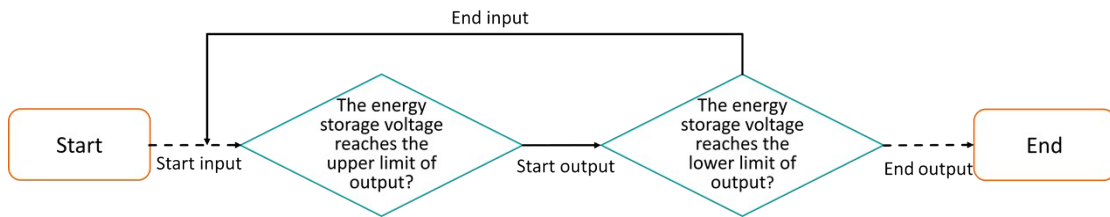
Supplementary Figure 11 Circuit schematic diagram. (A) Schematic of the PM electronics. (B) Schematic of the BLE electronics. (C) Schematic of the ACC electronics.



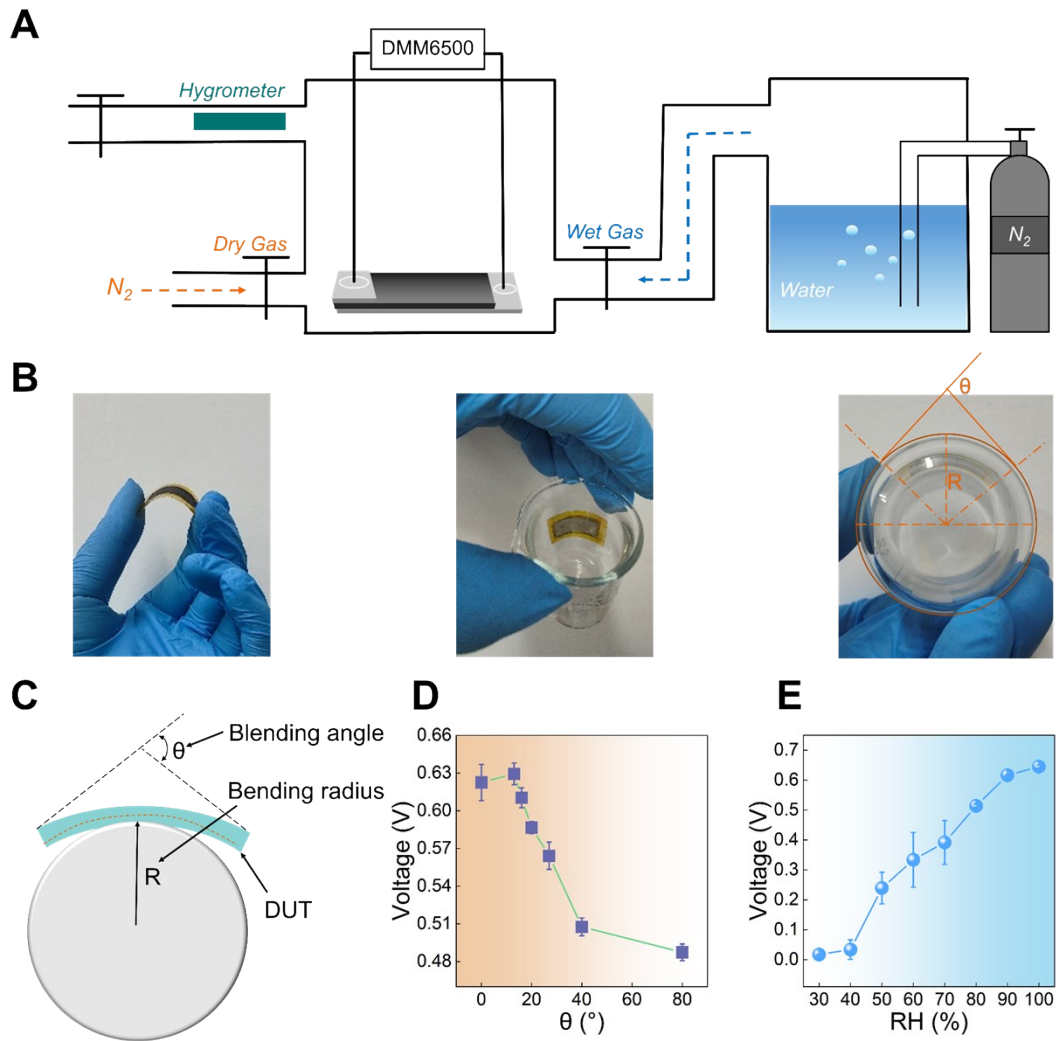
Supplementary Figure 12 System architecture and functional block diagram of the Bluetooth system in operation. (A) Minimal system in a chip-level package that includes a 32 MHz crystal oscillator, a DC-DC conversion network, a 1M Flash, an RF matching network, and an onboard antenna. (B) Software logic that is written by the Keil MDK.



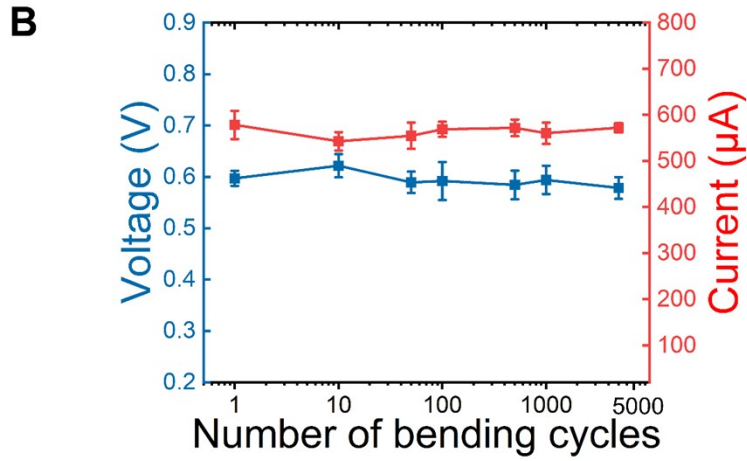
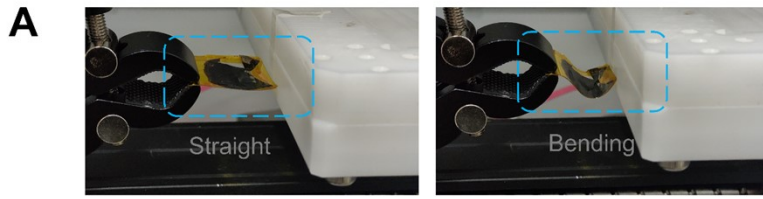
Supplementary Figure 13 Characterization and testing of energy management electronics.



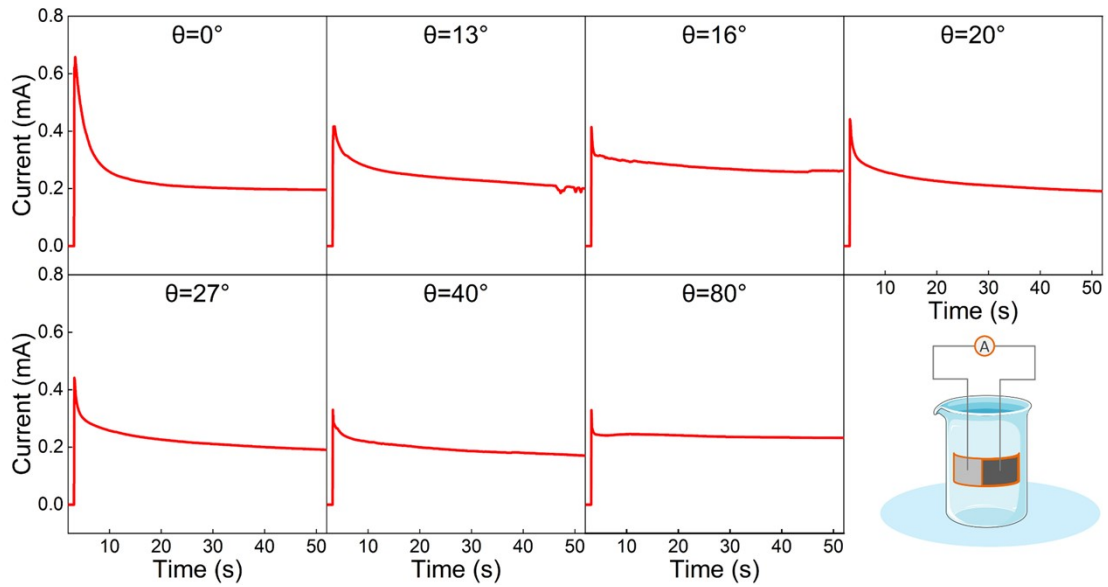
Supplementary Figure 14 Flow chart of energy management.



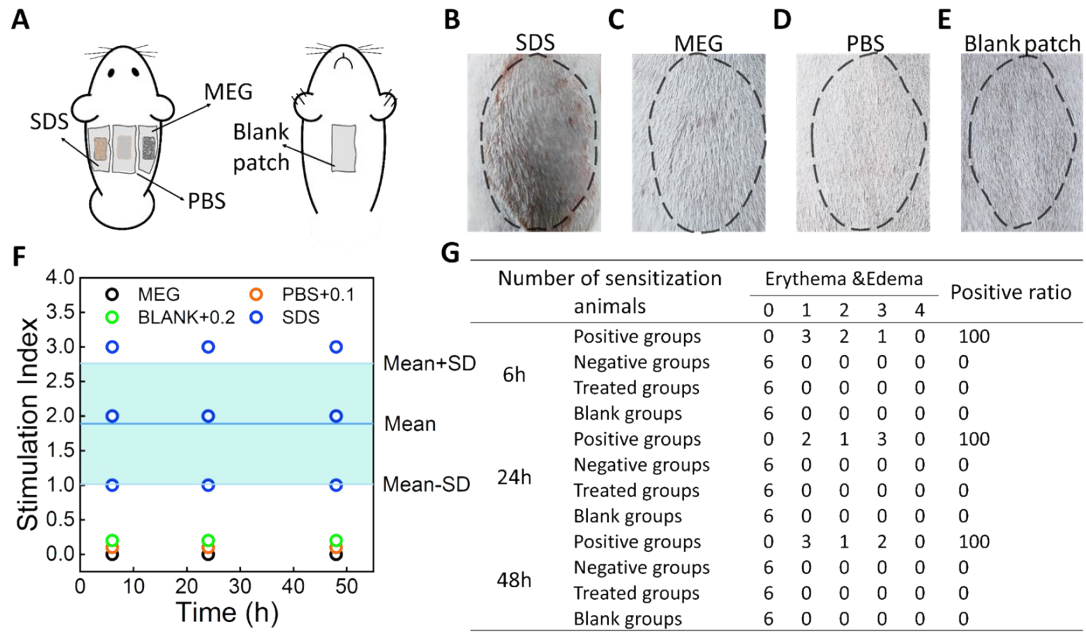
Supplementary Figure 15 Performance testing of MEG devices. (A) Humidity generation systems for testing the power generation effect of the MEG at specific humidity levels. This system provides a controlled test environment with relative humidity ranging from 50% to 100%. (B) Bending test: Various cup sizes are employed to test the electrical output of the MEG under different bending conditions. (C) Illustration of the bending test. DUT: Device under test. (D) Variation of voltage under different bending angles. (E) Variation of voltage under different ambient humidity.



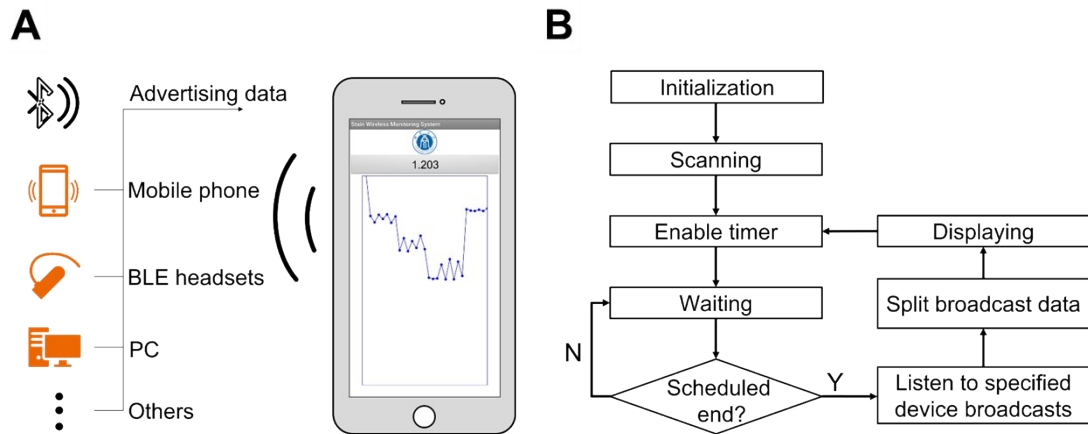
Supplementary Figure 16 Bending cycle test. (A) Device under test; (B) Electrical output after bending cycle.



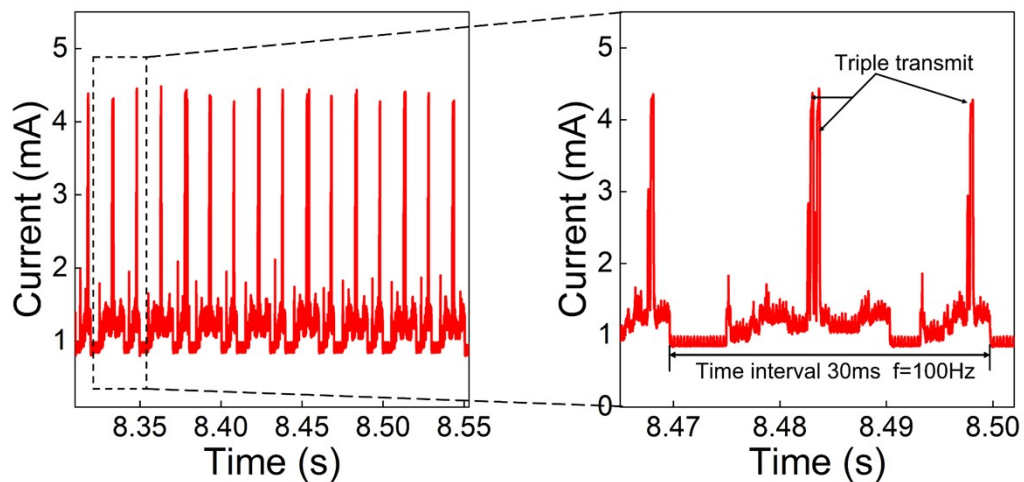
Supplementary Figure 17 Current output of a single device under different bending angles.



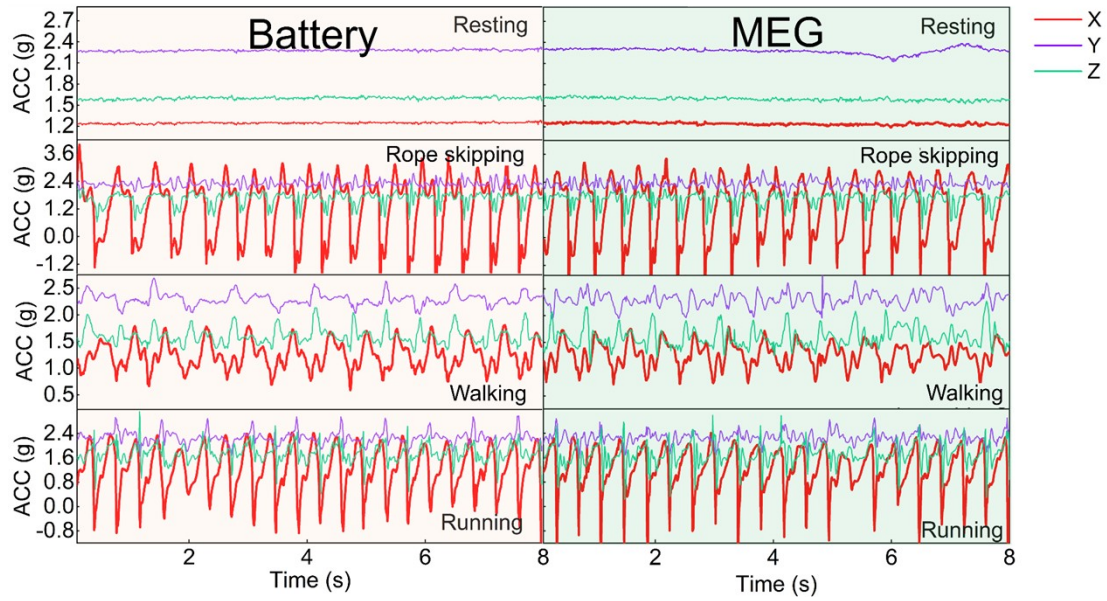
Supplementary Figure 18 Skin sensitization study of graphene oxide in guinea pigs. (A) Skin test area. Right side of the back: Treated group. Back: Negative group. Left side of the back: Positive group. Abdomen: Blank group. (B) Positive group. (C) Treated group. (D) Negative group. (E) Blank group. (F) The degree of stimulation over time. (G) The skin reaction scoring record.



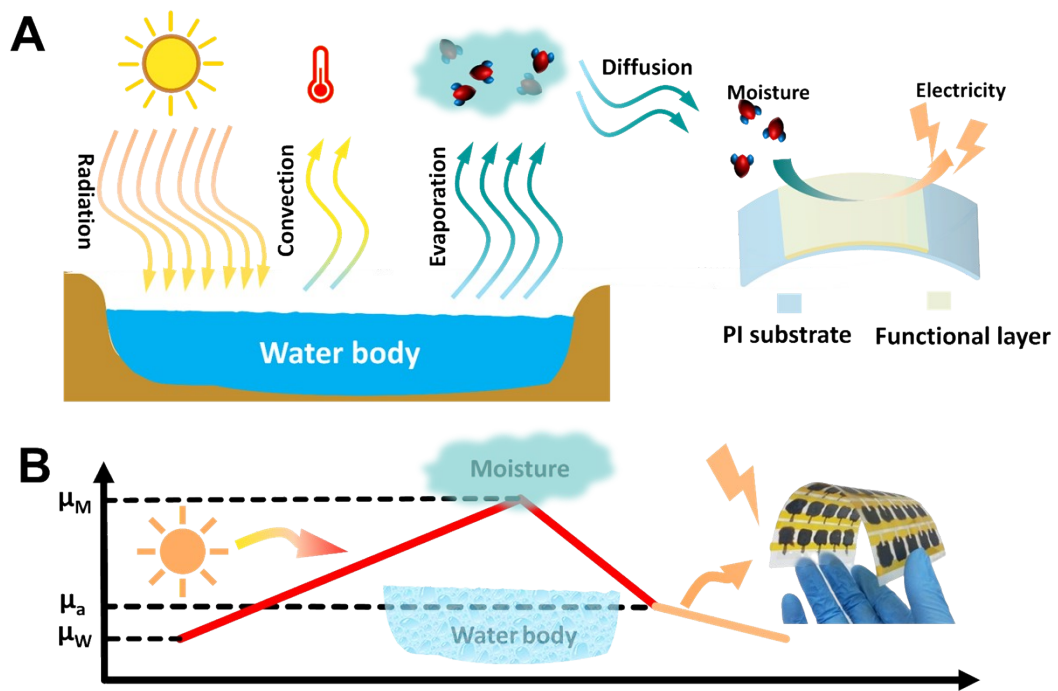
Supplementary Figure 19 Development and architecture of mobile applications and logical modules. (A) Illustration of the Mobile App processing various data received via Bluetooth. (B) Illustration of the BLE operation logic.



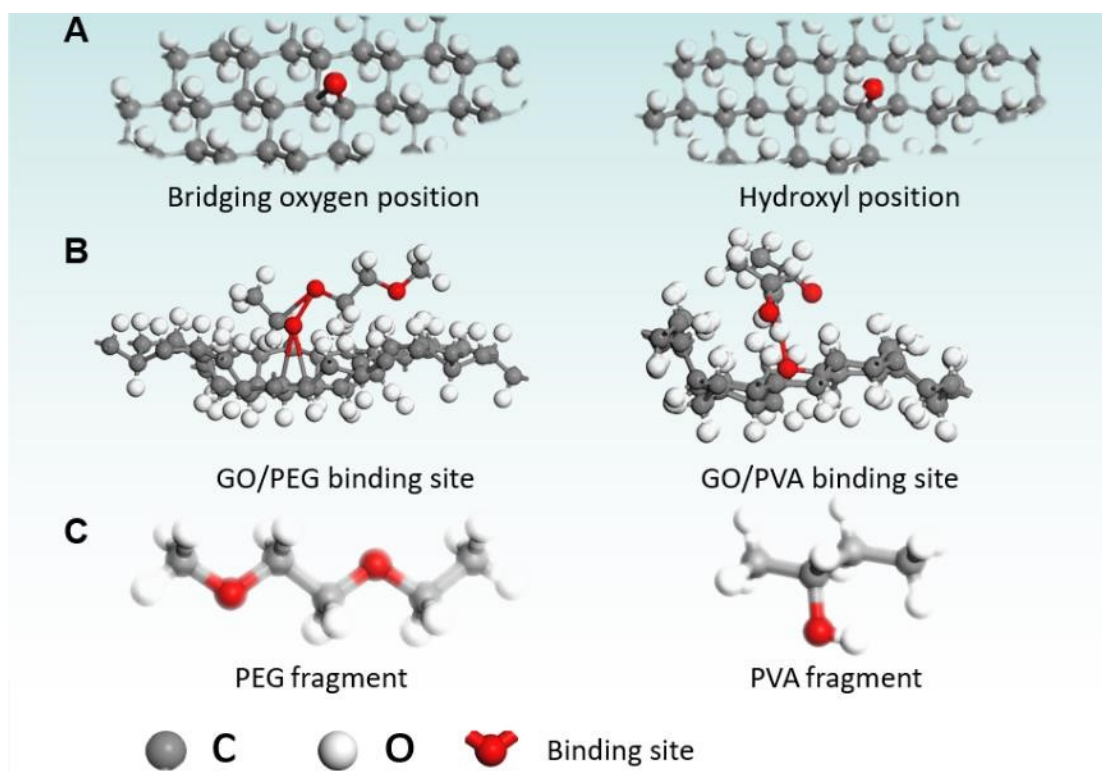
Supplementary Figure 20 Electrical current output during Bluetooth operation. (a) Time-histories of electric current during Bluetooth operation. (b) Zoom-in display of one working cycle.



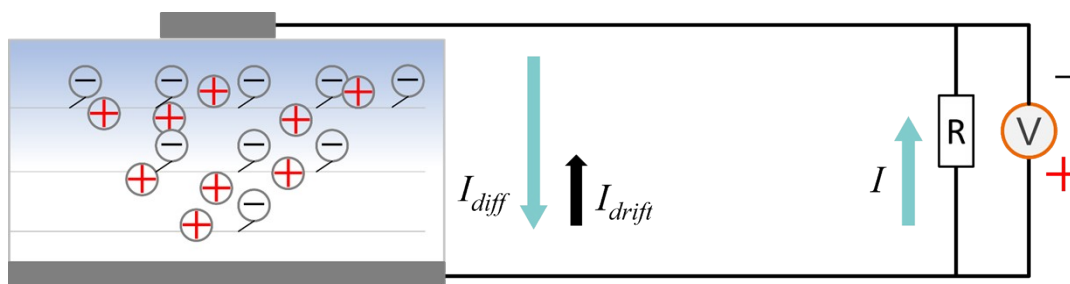
Supplementary Figure 21 Comparison of data differences between battery and MEG.



Supplementary Figure 22 Net changes in the power generation process. (A) The source of the energy that the MEG captures. (B) The energy balance is achieved through the input radiant energy, the output convection and evaporation.



Supplementary Figure 23 Theoretical determination of functionalized graphene oxide's structural and proton-binding properties using DFT calculations. (A) GO binding site. (B) GO/PEG binding site and GO/PVA binding site. (C) Binding fragments.



Supplementary Figure 24 The current in the device when the circuit is closed.

Table S1 Electrical performance comparison of various MEG devices.

Refs.	Substrate	Process	Functional layer Electrode		Electric output Per unit	Power density (W·m ⁻²)	Application scenarios
3	GO-film	Laser & annealing polarization	GO	rGO	0.15V, 0.5μA·cm ⁻²	7.5×10 ⁻⁴	/
4	P-rGO	Freeze-drying, forging & pressing	Reduced GO/GO	Au	0.45V, 0.9μA·cm ⁻²	4.05×10 ⁻³	LED
5	Device itself	Freeze-drying & tableting process	GO	Au/Ag	1.5V, 27.2nA·cm ⁻²	4.08×10 ⁻⁴	LED
6	Thermal-insulated plate	Sonication & freeze-dried	GO	Au/Ag	0.6V, 1.6μA·cm ⁻²	9.6×10 ⁻³	LED
7	Slide glass.	Slurry casting	PSSA/PAA-CMC/Carbon	Cu wire/Au	0.4V, 0.45μA·cm ⁻²	1.8×10 ⁻³	LED
8	Shell	Sonication & press process	GO	Au/Au	0.4V, 2μA·cm ⁻²	8×10 ⁻³	/
9	FTO glass	Printing & acid treatment	GO/PVA	Ag/FTO	0.85V, 92.8μA·cm ⁻²	0.78	Calculator
10	PET	Screen-printing	PDDA ink	C-Al	1.1V, 2.86μA·0.3cm ⁻²	0.104	Electronic watch
11	Paper	Printing	NaCl	Cu/Al	0.58V, 2.29μA	/	Sensor
12	Polyamide membrane	Print-coating	GO/PDDA	Ag/Cu	0.9V, 73μA·cm ⁻²	0.657	LED/ Capacitors
13	FTO	Coating	P ₂ W ₁₇ Cu	FTO/Cu	0.68V, 19.5μA·cm ⁻²	0.1326	/
14	Al foil	Freeze drying	12-ORC	Al	1.07V, 15.90nA	/	LED/Watch
15	metal-organic framework	Impregnation	LiCl/ Carbon black/PVA	Carbon tape/Au	0.78V, 7.5μA·cm ⁻²	5.85 ⁻²	LED/ Capacitors

16	Gold electrode	Freeze-drying	GO/SiO ₂	Au	0.5V, 100μA	0.12	LED
17	PET	Spray coated	PAN/Al ₂ O ₃	Porous carbon	3.18V	/	capacitors
This work	PET/PI	Scraper-pressure-coating	GO/PVA/PEG	Ag/Cu	0.614V, 625μA·cm ⁻²	3.01	BLE+ Acc sensor

Note: Direct current output MEGs. The humidity conditions from top to bottom are 80, 85, 80, 80, 20, 75, 70, 80, 91.5, 85, 90, 85, 65, 100, 32 and 90 (RH%).

Table S2 Binding energy comparison.

Fragments	GO-O	GO-OH	PEG	PVA	GO-O/PEG	GO-O/PVA	GO-OH/PEG	GO-OH/PVA
E(eV)	-60946.109	-60979.579	-9465.972	-6352.544	-70420.062	-67304.41	-70451.692	-67338.697
$E_{bind} = E_{complex} - (E_{molecule} + E_{GO})$								
Binding energy(eV)	GO-O/PEG	GO-O/PVA	GO-OH/PEG	GO-OH/PVA				
	-7.981	-5.757	-6.141	-6.574				

Table S3 Band gap results.

Fragments	GO-O	GO-OH	GO-O/PEG	GO-OH/PVA
Band gap	5.165eV	5.017eV	3.506eV	4.045eV

References

1. X. Liu, H. Gao, J. E. Ward, X. Liu, B. Yin, T. Fu, J. Chen, D. R. Lovley and J. Yao, *Nature*, 2020, **578**, 550-554.
2. J. Liu, L. Huang, W. He, X. Cai, Y. Wang, L. Zhou and Y. Yuan, *Nano Energy*, 2022, **102**, 107709.
3. C. Yang, Y. Huang, H. Cheng, L. Jiang and L. Qu, *Adv Mater*, 2019, **31**, e1805705.
4. H. Cheng, Y. Huang, F. Zhao, C. Yang, P. Zhang, L. Jiang, G. Shi and L. Qu, *Energy & Environmental Science*, 2018, **11**, 2839-2845.
5. Y. Huang, H. Cheng, C. Yang, P. Zhang, Q. Liao, H. Yao, G. Shi and L. Qu, *Nature Communications*, 2018, **9**, 4166.
6. Y. Huang, H. Cheng, C. Yang, H. Yao, C. Li and L. Qu, *Energy & Environmental Science*, 2019, **12**, 1848-1856.
7. S.-H. Shin, J. Y. Cheong, H. Lim, V. V. T. Padil, A. Venkateshaiah and I.-D. Kim, *Nano Energy*, 2020, **74**, 104827.
8. T. Xu, X. Ding, C. Shao, L. Song, T. Lin, X. Gao, J. Xue, Z. Zhang and L. Qu, *Small*, 2018, **14**, e1704473.
9. R. Zhu, Y. Zhu, F. Chen, R. Patterson, Y. Zhou, T. Wan, L. Hu, T. Wu, R. Joshi, M. Li, C. Cazorla, Y. Lu, Z. Han and D. Chu, *Nano Energy*, 2022, **94**.
10. T. He, H. Wang, B. Lu, T. Guang, C. Yang, Y. Huang, H. Cheng and L. Qu, *Joule*, 2023, **7**, 935-951.
11. Z. Duan, Z. Yuan, Y. Jiang, Q. Zhao, Q. Huang, Y. Zhang, B. Liu and H. Tai, *Chemical Engineering Journal*, 2022, **446**, 136910.
12. D. Maity and M. Fussenegger, 2023, **10**, 2300750.
13. T. Ji, W. Chen, Z. Kang and L. Zhang, *Nano Research*, 2023, DOI: 10.1007/s12274-023-5959-5.
14. L. Huang, Y. Zhang, X. Song, D. Li, X. Chen and Q. Yuan, *Nano Energy*, 2023, **118**, 108973.
15. J. Tan, S. Fang, Z. Zhang, J. Yin, L. Li, X. Wang and W. Guo, *Nature Communications*, 2022, **13**, 3643.
16. H. Wang, T. He, X. Hao, Y. Huang, H. Yao, F. Liu, H. Cheng and L. Qu, *Nature Communications*, 2022, **13**, 2524.
17. L. Li, Z. Zheng, C. Ge, Y. Wang, H. Dai, L. Li, S. Wang, Q. Gao, M. Liu, F. Sun and T. Zhang, 2023, **35**, 2304099.